Numerical Simulation Techniques for Damage Response Analysis of Composite Structures

Shirsendu Sikdar, Wim Van Paepegem, Wiesław Ostachowiczc, and Mathias Kersemans

Abstract Structural health monitoring (SHM) of composite structures plays an important role in nondestructive evaluation of safety-critical engineering applications. Elastic wave propagation based SHM techniques have proven their potential in effective assessment of structural discontinuities and damages. Numerical simulations play a significant role in development of robust SHM strategies for such composite structures. These simulations are experimentally validated for selected baseline cases and then applied to solve a panoptic range of plausible study cases, such as—variable operating conditions, increasing structural complexities, damage size and damage shapes. Thus, the numerical simulations can significantly help in reducing rigorous laboratory experimentations, saving time and cost. This chapter is mainly focused on the guided wave propagation and acoustic emission-based damage response analysis in fiber (graphite/glass/natural) reinforced composite structures used in the automotive, marine, wind-energy and aerospace industries. Based on the problem-solving efficiency and popularity, the spectral element and finite element method based numerical simulation technics are explicitly selected to be discussed here.

Keywords Composite structure · Damage · Guided wave propagation · Numerical simulation, acoustic emission · Acoustic emission · Structural health monitoring (SHM) · Piezoelectric transducer (PZT)

S. Sikdar (✉) · W. Van Paepegem · M. Kersemans
Mechanics of Materials and Structures (UGent-MMS), Department of Materials, Textiles and Chemical Engineering (MaTCh), Ghent University, Technologiepark-Zwijnaarde 46, 9052 Zwijnaarde, Belgium
e-mail: Shirsendu.Sikdar@UGent.be

W. Ostachowiczc
Institute of Fluid-Flow Machinery, Polish Academy of Sciences, 14, Fiszera Street, 80-231 Gdansk, Poland

M. Jawaid et al. (eds.), *Structural Health Monitoring System for Synthetic, Hybrid and Natural Fiber Composites*, Composites Science and Technology,
https://doi.org/10.1007/978-981-15-8840-2_7

1 Introduction

Lightweight fiber-reinforced composite structures (laminates and sandwiches) are of huge demand in automotive, aviation, marine and wind energy industries, due to their construction flexibilities, high in-plane strengths, high stiffness/weight ratios and damping capacities [1–5]. But, variable loading conditions (such as—abrasion, impact, fatigue) and hazardous ambient conditions (such as—moisture-content variation, temperature fluctuations) can eventually generates various types of damage (debond, delamination, fibre-cracking, localized inhomogeneity, breathing-cracks, amongst others) in these structures, and may grow further leading to a sudden failure of the structure while in service [6–11]. Therefore, development of nondestructive robust structural health monitoring (SHM) strategies are needed to identify the damage symptoms in advance. Some nondestructive evaluation techniques are proposed that uses the acoustic emission (AE), guided wave (GW) propagation, infrared-thermography, laser-vibrometry, X-ray computed tomography, ultrasonic goniometric-immersion methods for the inspection of composite structures [12–14]. The ultrasonic GW propagation and AE based SHM methods are popularly used for damage identification in composite structures [15–21].

Ultrasonic GW are elastic waves (e.g., Rayleigh wave, Lamb wave) that generate various wave modes while propagating in the structure. These SHM methods have the potential to detect minor structural defects in composite structures [6, 22–25]. The major advantages of these SHM methods are the capacity of GWs to penetrate hidden layers in the structures and the potential of large area inspection [26, 27].

AE is a sudden release of strain energy in the form of elastic waves that emitted due to the extension and initiation of damages in structures. These SHM techniques offer large-area inspection with limited instrumentation and give a clear idea about structural damage propagation and/or initiation events [21]. In these SHM techniques, the AE sensors register the wave motion owing to the damage in the materials and converts them to waveforms. Analysis of these waveforms can help to understand the intensity and the nature of damage. This technique has in-service monitoring potential without any external supplied excitations [28].

Numerical simulation of AE and GW propagation and their interaction with different types of damages in composite structures plays a vital role for the development of SHM strategies by giving the scope of exploring several possible case-studies without conducting physical experiments that significantly saves time and cost. The finite element simulations of GW propagation and AE in composites have established their capability to replicate the physical experiments for a wide range of study cases. In Patera [29], the spectral element simulation technique has introduced that flexibility and coalesces of finite element method with fast-convergences. Willberg [30] presented a study on the vantages of higher-order finite element method-based simulation techniques for the solution of elastodynamic problems. In these finite element simulations, a relatively finer discretization (min. 15 nodes per wavelength) is recommended. Whereas, the spectral element simulations can handle a relatively coarse discretization (min. 8 nodes per wavelength). The spectral element simulation

also offers the capacity to efficiently simulate the GW propagation in composites [27, 31–33]. This chapter presents some experimentally validated numerical simulations of AE and GW propagation in damaged composite structures.

2 Numerical Simulation Using Finite Element Method

Finite element simulations of damage induced AE and GW propagation and their interaction with damages in composite structures are presented by many researchers [3, 5, 7, 9]. These numerical simulations are usually carried out using popular finite element software, such as—Abaqus, ANSYS, COMSOL Multiphysics, LS-DYNA, Nastran, amongst others. Some experimentally validated simulation cases using Abaqus are described here.

2.1 Numerical Simulation of AE in Composites

Numerical simulation of damage-induced acoustic emission in a stiffened composite panel (SCP) can be carried out using the in Abaqus explicit analysis code. The SCP (500 mm × 500 mm × 2 mm) is made of carbon fibre composite laminate (CFCL) and it consists of 4-nos. of 500 mm long L-shaped (30 mm × 30 mm) stiffeners those bonded to the baseplate with epoxy adhesive, as presented in Fig. 1.

The three-dimensional (3D) SCP was modelled using 8-noded linear brick C3D8R elements of size (1 × 1 × 0.25) mm for the CFCL and (1 × 1 × 0.01) mm for the adhesive. Fixed boundary conditions (zero displacements and rotations) are assigned to the edges of the SCP. The assumed material properties of the CFCL and epoxy adhesive are given in Table 1.

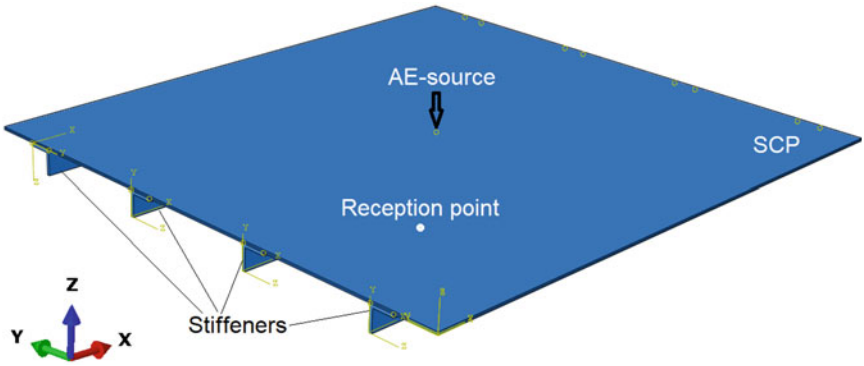

Fig. 1 Numerical model of the stiffened composite panel

Table 1 Material properties of stiffened composite panel

Material	E_{11} (GPa)	E_{22} (GPa)	E_{33} (GPa)	G_{12} (GPa)	G_{23} (GPa)	G_{13} (GPa)	ν_{12}	ν_{13}	ν_{23}	ρ (kg/m^3)
CFCL	76.02	76.02	9.85	3.77	3.35	3.35	0.03	0.36	0.36	1560
Adhesive	4.052	4.052	4.052	1.447	1.447	1.447	0.40	0.40	0.40	1100

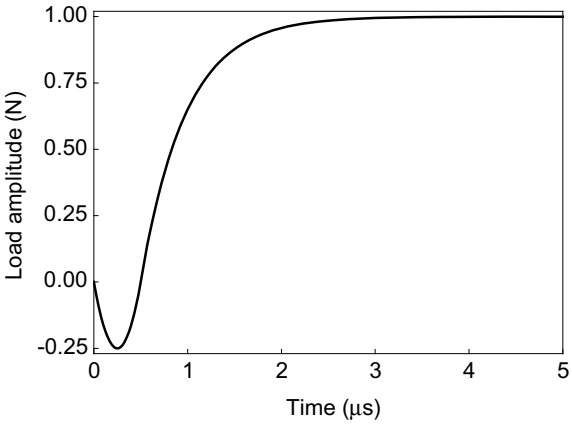

Fig. 2 Artificial AE-source for the simulation of acoustic emission in SCP

Selection of a proper loading-source is a vital component for simulation of AE in composite structures [34–36]. The cosine bell-function can be used for the simulation of artificial AE source that resembles a crack-like damage initiation in the structure [35]. The AE-source located at a point is described as

$$P(x_1, x_2, t) = p(t)\delta(x_1), \delta(x_2) \tag{1}$$

$$p(t) = \begin{cases} \frac{t(t-\tau)}{\tau^2}, & 0<t<\tau \\ 1-e^{-2.1(t-\tau)}, & t<\tau \end{cases} \tag{2}$$

where '$p(t)$' is the forcing-function, time-variable $t = 0 \rightarrow \tau$ and 'τ' represents rise-time of load and the AE source is a graphically represented in Fig. 2. In all simulation, a stable time-step of 1e−7 is considered.

The numerical AE signal collected at the 180 mm distant reception point (Fig. 1) from the applied AE source location is presented in Fig. 3. The waveform plot of a typical AE signal in Fig. 4 shows the generation and propagation of the AE signal in SCP.

2.2 Numerical Simulation of GW Propagation in Composites

Finite element simulation of ultrasonic GW propagation in an adhesively bonded composite structure with hidden disbond (bond failure) is described here. The simulation in Abaqus is carried using 0.5 mm thick and 10 mm diameter circular piezoelectric wafer transducer (PWTs) for GW signal actuation and reception in a bonded composite panel (BCP). The 7 mm thick BCP is made of two woven CFCL (300 mm × 300 mm × 3.5 mm) bonded with epoxy adhesive. An 8 mm dia. zero-volume

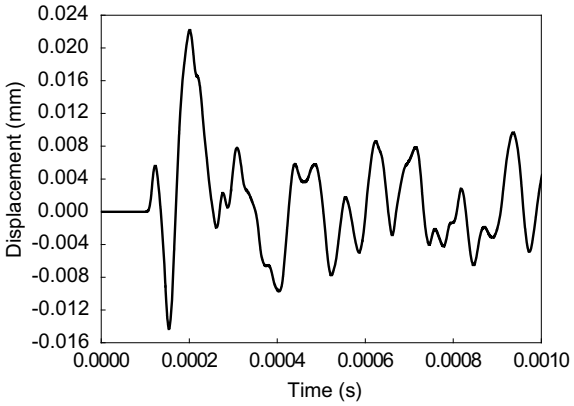

Fig. 3 AE signal registered at the reception point (Fig. 1)

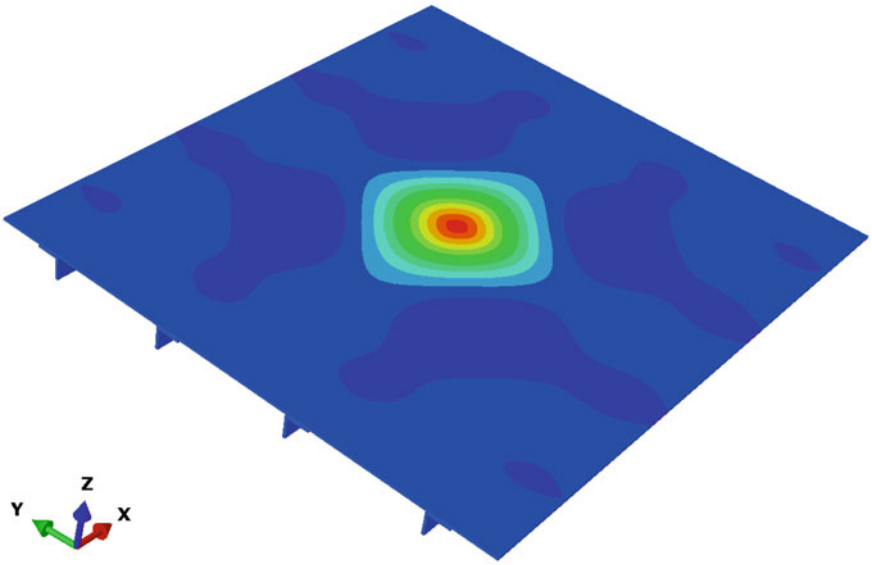

Fig. 4 Waveform of the AE signals in the SCP

disbond region was modelled in the BCP by undying the adhesive-to-top CFCL nodes at the adhesive layer, as shown in Fig. 5.

Numerical simulation of GW propagation in composites using actuator-sensor PWTs required the implicit and explicit solvers. In Abaqus, the implicit analysis solver is not effective to handle the transient analysis of elastic wave propagation in complex composite structures. Whereas, the explicit code can efficiently handle the GW propagation in such composites but, it has no provision for piezoelectric elements which is available in the implicit solver [37]. Therefore, GW in BCP is

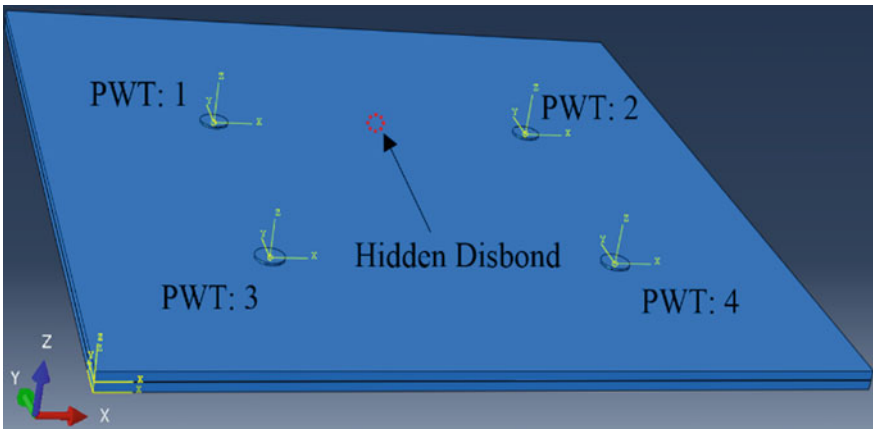

Fig. 5 Numerical model of the sample panel in Abaqus

modeled in explicit analysis solver and PWTs are modeled in the implicit analysis solver. The 'standard explicit co-simulation' is assigned to link the implicit and explicit analysis of wave propagation in BCP [37, 38].

In explicit modeling, the C3D8R elements are used and the layer-wise element sizes for CFCL and adhesive are considered as (0.5 × 0.5 × 0.25) mm and (0.5 × 0.5 × 0.01) mm, respectively. Whereas, in the implicit solver the PWTs (actuator/sensor) are modeled with the standard C3D8E linear piezoelectric brick elements (8-nodes, 6-degrees of freedom at each node) are selected. The C3D8E elements are capable to handle the electro-mechanical coupling of the PWTs, where the 'voltage' is assigned as an additional degree of freedom in those coupling elements. A preselected input of 150 kHz 5-cycle sine wave signal in Hanning-window described in Fig. 6 is applied

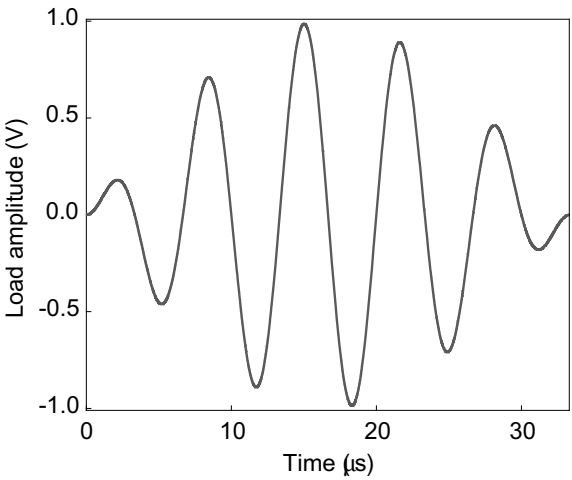

Fig. 6 Input signal for the actuator PWTs in the BCP

to the front-surface nodes of the actuators (PWT: 1 and PWT: 3), and zero voltage is assigned to the back-surface nodes of the actuators as well as sensors (PWT: 2 and PWT: 4) for grounding operation.

The output signal (in terms of voltage) is registered at the front-surfaces of sensors (PWT 2 and PWT 4). The PWT (NCE51) properties are assumed as:

$$[\varepsilon] = \begin{bmatrix} 1.72 & 0 & 0 \\ & 1.72 & 0 \\ \text{Symmetry} & & 1.68 \end{bmatrix} \times 10^{-8}\,\text{C/Vm},$$

$$[e] = \begin{bmatrix} 0 & 0 & 0 & 0 & 13.7 & 0 \\ 0 & 0 & 0 & 13.7 & 0 & 0 \\ -6.06 & -6.06 & 17.2 & 0 & 0 & 0 \end{bmatrix} \text{C/m}^2,$$

$$[c] = \begin{bmatrix} 13.4 & 8.89 & 9.09 & 0 & 0 & 0 \\ & 13.4 & 9.09 & 0 & 0 & 0 \\ & & 12.1 & 0 & 0 & 0 \\ & & & 2.05 & 0 & 0 \\ & & & & 2.05 & 0 \\ & & \text{Symmetry} & & & 2.24 \end{bmatrix} \times 10^{10}\,\text{N/m}^2$$

where $[\varepsilon]$ represents piezoelectric permittivity-matrix, $[e]$ represents piezoelectric stress-matrix, $[c]$ is the tensor of mechanical-stiffness, and the piezoelectric material mass-density 'ρ' is 7650 kg/m^3. In the simulation, the time-step was considered as $\leq$1e$-$7 (less than the minimum distance of any node-to-node connection/the maximum achievable velocity of the GW mode).

In the numerical simulation, the PWT#1 is actuated with the input signal and the propagated signal is collected at PWT#2 to get the without-disbond signal corresponding to the PWT actuator-sensor path#1-2. Similarly, PWT#3 is actuated and the signal at PWT#4 is registered to get the with-disbond signal from PWT actuator-sensor path#3-4. A comparison of those without-disbond signal and with disbond signal is shown in Fig. 7. The numerically obtained waveform plot in Fig. 8 indicates the disbond influence on the propagating GW signals in BCP.

3 Numerical Simulation Using Spectral Element Method

The spectral element simulation also offers the potential to solve the ultrasonic GW propagation problems in composites [31, 32]. A time-domain spectral element simulation of GW propagation in the sample BCP is carried out in MATLAB using 100 kHz 5-cycle tone-burst sine wave, as presented in Fig. 9.

This spectral element analysis technique has some similarities with the finite element method (Sect. 2.2) except in the node distributions and in the approximation functions those resembles the changes in displacements calculated during the

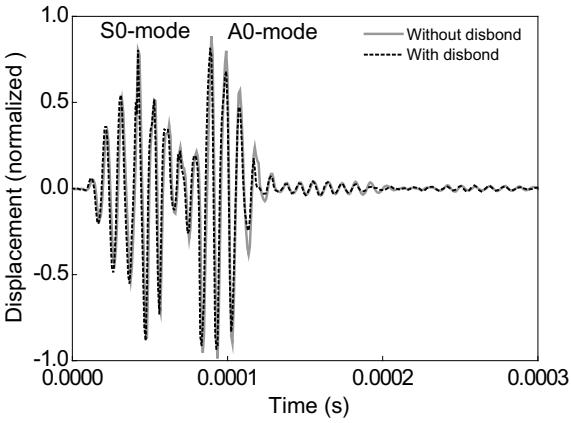

Fig. 7 Comparison of GW signals corresponding to the without and with disbond paths

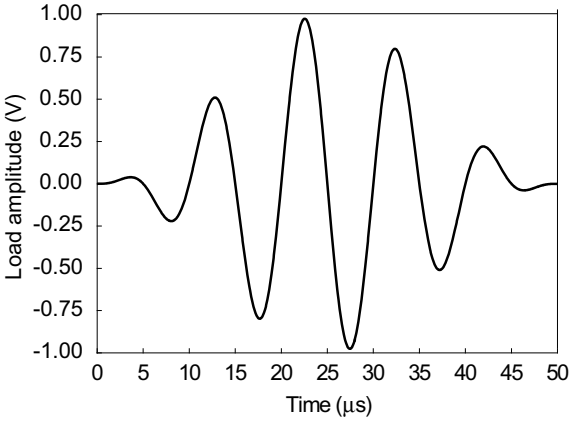

Fig. 8 Waveform plot shows the disbond effect in the propagated GWs in the BCP

simulation. The nodes are non–uniformly distributed in spectral elements and their locations can be obtained by evaluating the roots (real values) of 'ξ_i' as

$$\left.\begin{aligned}\left\{\left(1-\xi^2\right)U'_{a-1}(\xi)\right\}=0\\ \left\{\left(1-\eta^2\right)U'_{b-1}(\eta)\right\}=0\\ \left\{\left(1-\varsigma^2\right)U'_{c-1}(\varsigma)\right\}=0\end{aligned}\right\rangle \tag{3}$$

where the *Legendre polynomials are represented as* ξ, η, ζ, ϵ $[-1; 1]$, U_{a-1}, U_{b-1}, U_{c-1}; the number of nodes along ξ, η, ζ directions are represented as *a, b, c* and the first-derivatives are indicated with '′'. The shape function (3D) is formulated by using the tensor product of 1D shape functions with Lagrange polynomials $N_j(\xi)$, $N_k(\eta)$,

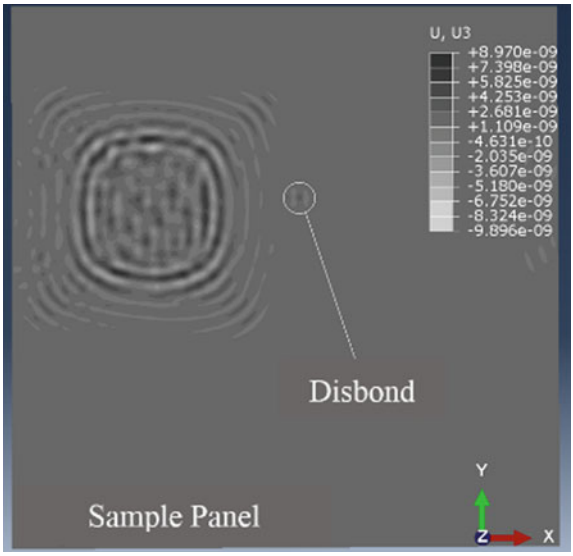

Fig. 9 Input signal for the actuator PWTs in the BCP

$N_l(\varsigma)$ of degree $(a-1)$, $(b-1)$, $(c-1)$ as described in Fig. 10. The polynomials are represented as:

$$N_p(\xi, \eta, \varsigma) = N_j(\xi) N_k(\eta) N_l(\varsigma) \tag{4}$$

in which, $j = 1 \rightarrow a, k = 1 \rightarrow b \text{and} l = 1 \rightarrow c$.

The *Gauss Lobato Legendre* (GLL) integration technique is applied to compute the element matrices, where these integration points coincide with selected number of spectral nodes. The quadrature of GLL is a product of one-dimentional quadrature with weights of p_j, p_k, p_l as

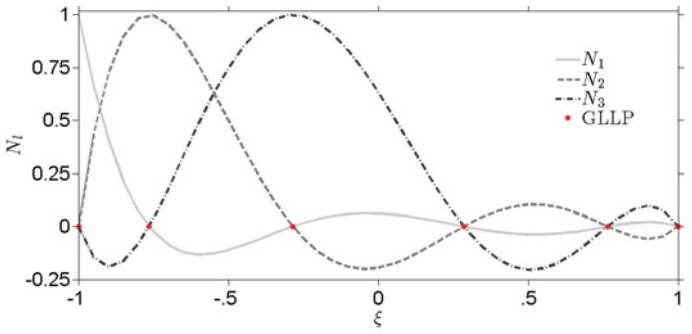

Fig. 10 Graphical presentation of the shape functions ($N_i(\xi)$)

$$\left.\begin{aligned} p_j &= \frac{2}{a(a-1)\left(U_{a-1}(\xi_j)\right)^2} \\ p_k &= \frac{2}{b(b-1)\left(U_{b-1}(\eta_k)\right)^2} \\ p_l &= \frac{2}{c(c-1)\left(U_{c-1}(\varsigma_l)\right)^2} \end{aligned}\right\rangle \tag{5}$$

Constitutive equation for the linear-piezoelectric materials can be represented as per Giurgiutiu and Lyshevski [39]

$$\begin{Bmatrix} \sigma \\ D \end{Bmatrix} = \begin{bmatrix} B^F & -e^T \\ e & \varepsilon^X \end{bmatrix} \begin{Bmatrix} X \\ f \end{Bmatrix} \tag{6}$$

where the tensors 'ε^X' represents *dielectric* components, 'B^F' represents elastic components, 'e' represents *piezoelectric* components, 'F' is corresponding to the electrical-field constants, 'D' is corresponding to the electrical-displacements, 'σ' is the stress and 'X' is corresponding to the strains. The initial electric-fields, initial strains and transpose matrix are represented by the superscripts 'F', 'X' and 'T', respectively. The elementary governing equation of motion can be defined as:

$$\begin{bmatrix} m^e_{uu} & 0 \\ 0 & 0 \end{bmatrix} \begin{Bmatrix} \ddot{u}^e \\ \ddot{\varphi}^e \end{Bmatrix} + \begin{bmatrix} c^e_{uu} & 0 \\ 0 & 0 \end{bmatrix} \begin{Bmatrix} \dot{u}^e \\ \dot{\varphi}^e \end{Bmatrix} + \begin{bmatrix} k^e_{uu} & k^e_{u\varphi} \\ k_{u\varphi}{}^{eT} & k^e_{\varphi\varphi} \end{bmatrix} \begin{Bmatrix} u^e \\ \varphi^e \end{Bmatrix} = \begin{Bmatrix} F^e \\ G^e \end{Bmatrix} \tag{7}$$

where 'm^e_{uu}' represents structural mass-matrix, 'k^e_{uu}' represents stiffness-matrix, 'c^e_{uu}' represents damping-matrix, '$k^e_{\varphi\varphi}$' represents dielectric permittivity-matrix, '$k^e_{u\varphi}$' is piezoelectric coupling-matrix, 'φ^e' is electric potential vector, 'u^e' is nodal displacement-vector, 'F^e' is the external force-vector, 'G^e' represents the applied charge vector, and c^e_{uu} is defined based on the *damping model* by *Rayleigh in* [31] as

$$c^e_{uu} = \mu_m m^e_{uu} + \lambda_k k^e_{uu} \tag{8}$$

where 'λ_k' is the coefficient of stiffness proportionality and 'μ_m' is the mass-proportionality coefficients. The computation time is reduced by applying a central-difference scheme to solve Eq. (7).

A numerical model of PWT-induced GW propagation in BCP is presented in Fig. 11. The assumed material properties of BCP is given in Table 1. The PWT properties are selected as per the manufacturer's (*Noliac NCE51*) data (Sect. 2.2). In the simulation, the BCP and PWTs are modeled with 108 noded 3D spectral elements (36 in-plane nodes and 3-through thickness nodes), as schematically represented in Fig. 12. Each PWT element nodes has three displacement DOFs with one additional DOF (i.e. electric-voltage).

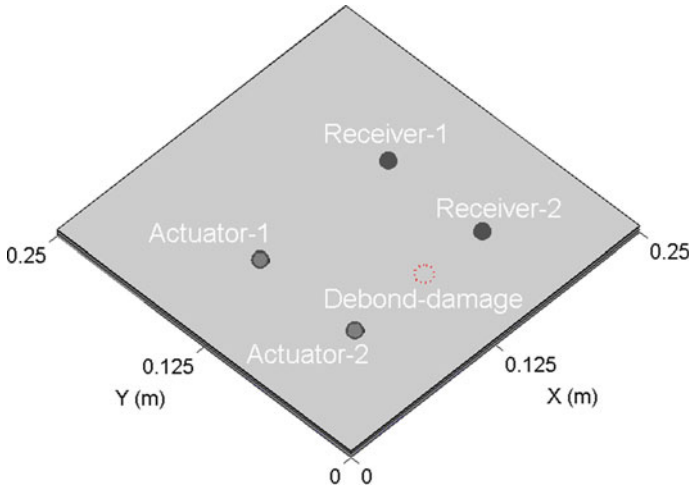

Fig. 11 Numerical model of BCP with PWTs

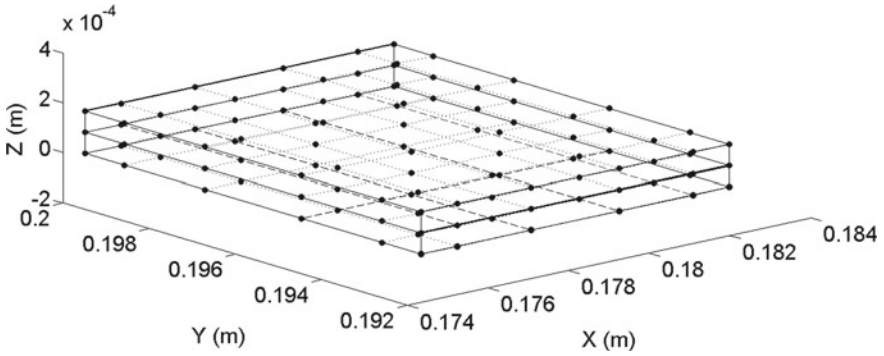

Fig. 12 Schematic of node distribution in the 3D spectral element

In each layer, there are 3500 number of in-plane elements and 24 number of elements in PWTs are connected to the front-layer of the BCP. The contact effect is not considered in simulation and a debond region of 8 mm diameter is modeled by demerging the adjoining nodes at the bond-layer (Fig. 12). The simulation was carried out in MATLAB and the time-step of calculation was selected as 1e−7. A comparison between the without-debond (signal corresponding to Actuator-1–Receiver-1) and with-debond (signal corresponding to Actuator-2–Receiver-2) is presented in Fig. 13 and a waveform plot is shown in Fig. 14 that shows the debond influence on the propagated GWs.

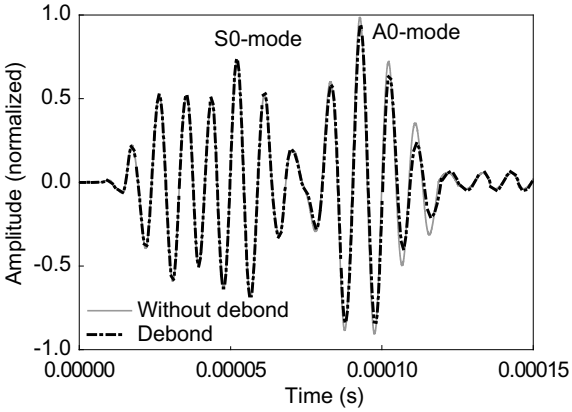

Fig. 13 Comparison of without debond and debond-influenced signals

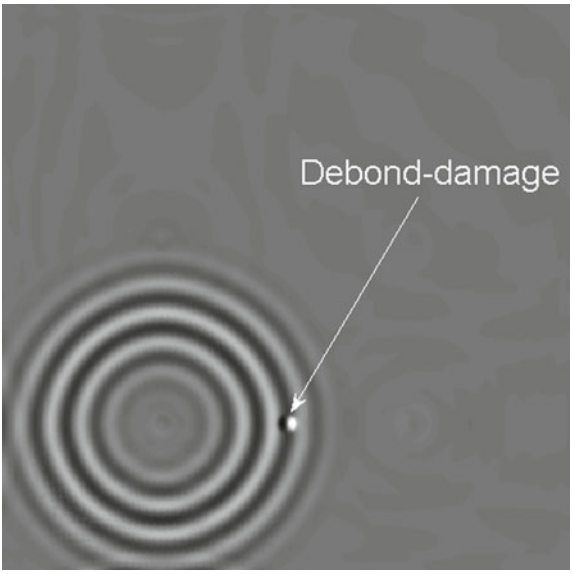

Fig. 14 Waveform plot from the simulation of BCP model indicates debond effect on the propagated GWs

4 Conclusions

This study is an effort to provide insights on the numerical simulation techniques for damage-induced AE as well as the PWT-induced GW propagation and interactions with damages in composite structures. It evident that the numerical simulations can give the insights about the damages in composites and can significantly contribute to the development of robust SHM strategies that use the AE and/or GW propagation-based nondestructive evaluation techniques. The finite element simulation of AE in a composite structure is quite straightforward and requires a proper artificial AE-source function to replicate the damage-source. This simulation technic can be used

for the solution of a wide range of laboratory-scale AE problems. This method is also suitable for simulation of ultrasonic GW propagation in composites with hidden damages (such as debond/disbond), using PWTs (actuators/sensors). The spectral element method-based simulation technique can be applied for fast and efficient simulation of elastic waves and damage response estimation in composite structures. It is expected that the given information will help the readers to understand the numerical simulation techniques and their applicability for different types of damage response analysis for composite structures.

Acknowledgements The wish to acknowledge the support from the Polish National Science Centre (NCN) Poland under agreement no. UMO.2018/29/B/ST8/02904 and the Research Foundation-Flanders (FWO) Belgium under agreement no. FWO.3E0.2019.0102.01.

References

1. Peters ST (1998) Handbook of composites. Chapman and Hall, Boca Raton, FL
2. Gay D, Hoa SV, Tsai SN (2003) Composite materials: design and application. CRC, New York
3. Sikdar S, Banerjee S (2017) Structural health monitoring of advanced composites using guided waves. LAP LAMBERT Academic Publishing, Saarbrücken
4. Safri SN, Sultan MT, Jawaid M, Jayakrishna K (2017) Impact behaviour of hybrid composites for structural applications: a review. Compos B Eng 133:112–121
5. Giurgiutiu V, Zagrai AN, Bao JJ (2002) Piezoelectric wafer embedded active sensors for aging aircraft structural health monitoring. Struct Health Monit 1:41–61
6. Hay TR, Wei L, Rose JL (2003) Rapid inspection of composite skin-honeycomb core structures with ultrasonic guided waves. J Compos Mater 37(10):929–939
7. Sikdar S, Kudela P, Radzieński M, Kundu A, Ostachowicz W (2018) Online detection of barely visible low-speed impact damage in 3D-core sandwich composite structure. Compos Struct 185:646–655
8. Maslov KI, Kundu T (1996) Selection of lamb modes for detecting internal defects in laminated composites. Ultrasonics 35:141–150
9. Mitra M, Gopalakrishnan S (2016) Guided wave based structural health monitoring: a review. Smart Mater Struct 25(5):053001
10. Wandowski T, Malinowski PH, Ostachowicz WM (2016) Circular sensing networks for guided waves based structural health monitoring. Mech Syst Signal Process 66:248–267
11. Yang B, Xuan FZ, Xiang Y, Li D, Zhu W, Tang X, Xu J, Yang K, Luo C (2017) Lamb wave-based structural health monitoring on composite bolted joints under tensile load. Materials 10(6):652
12. Li Y, Yang ZW, Zhu JT, Ming AB, Zhang W, Zhang JY (2016) Investigation on the damage evolution in the impacted composite material based on active infrared thermography. NDT&E Int 83:114–122
13. Castellano A, Fraddosio A, Piccioni MD (2017) Ultrasonic goniometric immersion tests for the characterization of fatigue post-LVI damage induced anisotropy superimposed to the constitutive anisotropy of polymer composites. Compos B Eng 116:122–136
14. Jespersen KM, Zangenberg J, Lowe T, Withers PJ, Mikkelsen LP (2016) Fatigue damage assessment of uni-directional non-crimp fabric reinforced polyester composite using X-ray computed tomography. Compos Sci Technol 136:94–103

15. Prosser WH (1996) Advanced AE techniques in composite materials research. J Acoust Emission 14:1–11
16. Wevers M (1997) Listening to the sound of materials: acoustic emission for the analysis of material behavior. NDT&E Int 30:99–106
17. Giordano M, Calabro A, Exposito C, D'Amore A, Nicolais L (1998) An acoustic-emission characterization of the failure modes in polymer composite materials. Compos Sci Technol 58:1923–1928
18. Green ER (1998) Acoustic emission in composite laminates. J Nondestr Eval 17:117–127
19. Bussiba A, Kupiec M, Ifergane S, Piat R, Bohlke T (2008) Damage evolution and fracture events sequence in various composites by acoustic emission technique. Compos Sci Technol l68:1144–1155
20. Unnthorsson R, Runarson TP, Jonsson MJ (2008) Acoustic emission based failure criterion for CFRP. Int J Fatigue 30:11–20
21. Wevers M, Lambrighs K (2009) Applications of acoustic emission for SHM: a review. Encyclopedia of structural health monitoring. Wiley, New York
22. Mustapha S, Ye L (2015) Propagation behaviour of guided waves in tapered sandwich structures and debonding identification using time reversal. Wave Motion 57:154–170
23. Pieczonka L, Ukowski P, Klepka A, Staszewski WJ, Uhl T, Aymerich F (2014) Impact damage detection in light composite sandwich panels using piezo-based nonlinear vibro-acoustic modulations. Smart Mater Struct 23(10):105021
24. Luchinsky DG, Hafiychuk V, Smelyanskiy VN, Kessler S, Walker J, Miller J, Watson M (2013) Modeling wave propagation and scattering from impact damage for structural health monitoring of composite sandwich plates. Struct Health Monit 12(3):296–308
25. He F, Zhou Z, Feng Z (2008) Research on an inspection method for de-bond defects in aluminum skin-honeycomb core sandwich structure with guided waves. In: 17th world conference on nondestructive testing
26. Lowe MJ, Challis RE, Chan CW (2000) The transmission of Lamb waves across adhesively bonded lap joints. J Acoust Soc Am 107(3):1333–1345
27. Ostachowicz W, Kudela P, Krawczuk M, Zak A (2011) Guided waves in structures for SHM: the time-domain spectral element method. Wiley, New York
28. Ono K, Gallego A (2012) Research and application of AE on advanced composite. J Acoust Emission 180–229
29. Patera AT (1984) A spectral element method for fluid dynamics: laminar flow in a channel expansion. J Comput Phys 54(3):468–488
30. Willberg C, Duczek S, Perez JV, Schmicker D, Gabbert U (2012) Comparison of different higher order finite element schemes for the simulation of Lamb waves. Comput Methods Appl Mech Eng 241:246–261
31. Kudela P, Żak A, Krawczuk M, Ostachowicz W (2007) Modelling of wave propagation in composite plates using the time domain spectral element method. J Sound Vib 302(4–5):728–745
32. Kudela P (2016) Parallel implementation of spectral element method for Lamb wave propagation modeling. Int J Numer Meth Eng 106(6):413–429
33. Ha S, Chang FK (2009) Optimizing a spectral element for modeling PZT-induced Lamb wave propagation in thin plates. Smart Mater Struct 19(1):015015
34. Sause MG (2011) Investigation of pencil-lead breaks as acoustic emission sources. J Acoust Emission 29
35. Mal AK, Banerjee S (2004) Guided acoustic emission waves in a thick composite plate. In Health monitoring and smart nondestructive evaluation of structural and biological systems III. Int Soc Opt Photon 5394:42–53
36. Banerjee S, Mal AK (2005) Acoustic emission waveform simulation in multilayered composites. J Strain Anal Eng Des 40(1):25–32
37. Soorgee MH, Lissenden CJ, Rose JL, Yousefi-Koma A (2013) Planar guided waves for SHM of plate structures using piezoelectric fiber transducers. AIP Conf Proc 1511:254–261

38. Sikdar S, Banerjee S (2016) Identification of disbond and high density core region in a honeycomb composite sandwich structure using ultrasonic guided waves. Compos Struct 152:568–578
39. Giurgiutiu V, Lyshevski SE (2016) Micro mechatronics: modeling, analysis, and design with MATLAB. CRC Press, New York